

A topology optimisation of composite elastic metamaterial slabs based on the manipulation of far-field behaviours

Kei Matsushima Hiroshi Isakari Toru Takahashi
Toshiro Matsumoto

July 15, 2020

Abstract

We propose a numerical method for a topology optimisation of composite elastic metamaterial slabs. We aim to realise some anomalous functionalities such as perfect absorption, wave-mode conversion, and negative refraction by designing the shape and topology of (visco-) elastic inclusions. Instead of manipulating effective material constants, we propose to utilise the far-field characteristics of scattered waves. This allows us to achieve novel functionalities for waves in not only low but also high-frequency ranges. The design sensitivity corresponding to the far-field characteristics is rigorously derived using the adjoint variable method and incorporated into a level-set-based topology optimisation algorithm. The design sensitivity is computed by the boundary element method with periodic Green's function instead of the standard finite element method to rigorously deal with the radiation of scattered waves without absorbing boundaries. We show some numerical examples to demonstrate the effectiveness of the proposed method.

Keywords Topology optimisation, Elastic metamaterial, Boundary element method, Periodic scattering, Topological derivative

1 Introduction

It is well known that electromagnetic waves exhibit extraordinary behaviours when they propagate through artificially designed periodic structures, such as electromagnetic metamaterials [1], metasurfaces [2], and photonic crystals [3]. Similar phenomena can be observed when elastic waves propagate in a medium whose mass density and elastic moduli are periodically arranged. For example, the elastic counterparts of the electromagnetic metamaterials are called elastic metamaterials [4], where an elastic wave behaves as if the medium has negative elastic moduli and/or a negative mass density.

As with the electromagnetic metamaterials, elastic metamaterials potentially possess unique functionalities that can help realise innovative wave devices. For example, negative material constants induce elastic wave cloaking [5, 6] and superlensing effects [7]. The locally resonant metamaterials [8] are another type of interesting material, which exhibit extremely low frequency band gaps. Furthermore, recent works have found that perfect mode conversion, which converts

an incident P-wave into S-waves or vice versa, is possible when the structure is designed carefully [9]. These anomalous properties can be beneficial in further improving vibration control and non-destructive testing technologies.

Topology optimisation is one of the most sophisticated tools for designing structures with desirable features and has been applied in various fields of science and engineering. Recent works have proposed some topology optimisation methods for manipulating elastic waves. After Sigmund and Jensen [10] designed phononic crystals with large bandgaps by using a topology optimisation based on a density-based method [11], many works have been devoted to maximising phononic bandgaps [12, 13, 14]. Jensen [15] studied the reflection and dissipation of elastic waves from periodic scatterers and optimised them to transmit or dissipate an incident wave within a target frequency range. Christiansen and Sigmund [16] utilised a topology optimisation to manipulate a scattering profile in an observation area and realised negative refraction using a metamaterial slab. Noguchi et al. [17], Yang and Kim [18], and Matsushima et al. [19] designed metasurfaces and metamaterial slabs exhibiting mode conversion in elastic systems. Dong et al. [20, 21, 22] proposed topology optimisations for designing elastic and acoustic metamaterials with broadband double-negative material constants. More comprehensive investigations on topology optimisation of phononic crystals and acoustic/elastic metamaterials were conducted by [23, 24].

These studies, however, aim to manipulate the indirect physical quantities such as bandgaps, effective material properties, and displacement distribution in a fixed observation domain. The effective parameters accurately describe wave propagation within the homogenised material only when the frequency is sufficiently low. The bandgap structures provide only a little information on the characteristics of waves propagating through a structure of finite thickness. In addition, introducing the observation domain produces an ambiguity regarding the manner the domain should be determined, which may adversely affect the performance of topology optimisation.

Recently, the authors proposed a new objective functional for topology optimisation that designs single-phase elastic metamaterial slabs [19]. Our objective functional was formulated by using the so-called far-field characteristics of elastic waves. Assuming spatial periodicity, we observed that scattered waves are expressed as a superposition of some plane waves. Then it turned out that their amplitudes are exactly written as a boundary integral of displacement and traction along the surface of a single scatterer. This implies that the boundary integral contains sufficient information for describing periodic scattering.

This study is an extension of our previous work [19]; herein, we aim to establish the topology optimisation of two-phase composite elastic metamaterial slabs. Achieving this objective allows us to not only improve design flexibility but also realise novel metamaterials that cannot be achieved by a single material, including an elastic wave absorber consisting of an elastic-viscoelastic composite material.

To this end, we aim to derive and compute a design sensitivity corresponding to our objective functional. Following our previous work [19], we employ a level-set-based algorithm [25, 26], which uses a topological derivative [27] as the design sensitivity. The topological derivative, however, cannot be derived in a standard manner (e.g. [28]) because our objective functional explicitly depends on the topology of scatterers. We suggest an alternative approach to rigor-

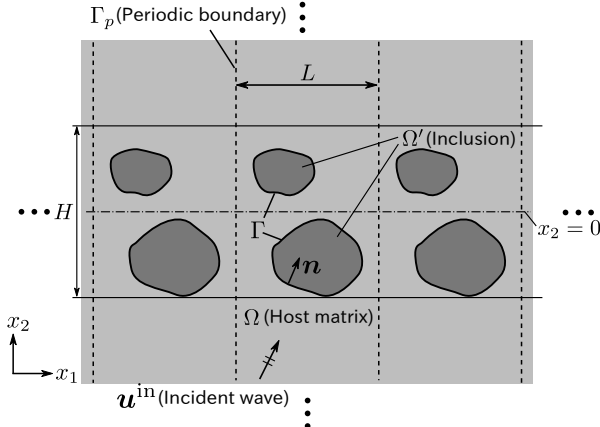


Figure 1: Model of the elastic metamaterial slab. The host matrix consists of lossless elastic material, where the inclusions may be viscoelastic. The inclusions are periodically allocated along the x_1 -direction and can exist in a finite strip $|x_2| < H/2$, where $H > 0$ represents a thickness of the slab

ously derive the topological derivative using a reciprocal theorem. To compute the topological derivative, we use the boundary element method (BEM) with periodic Green's function [19] instead of the standard finite element method, because BEM can rigorously deal with the radiation of scattered waves without absorbing boundaries such as the perfectly matched layer.

This paper is organised as follows. We first describe the model of elastic metamaterial slabs to be optimised and formulate periodic scattering in Section 2. Then, we explain our topology optimisation algorithm and derive the topological derivative in Section 3. In Section 4, using some numerical examples, we demonstrate that our topology optimisation can design elastic metamaterial slabs that exhibit perfect absorption, wave-mode conversion, and negative refraction. Finally, we conclude our study in Section 5.

2 Formulation

2.1 Elastic wave scattering by periodic inclusions

We consider a linear, isotropic, and homogeneous elastic matrix and (visco-) elastic inclusions characterised by the mass densities ρ and ρ' , and Lamé's constants (λ, μ) and (λ', μ') , respectively. The host matrix and inclusions are assumed to be under a plane-strain state and subject to a time-harmonic oscillation. The time dependence of the oscillation is chosen as $e^{-i\omega t}$, where $\omega > 0$ is the angular frequency, t denotes time, and i is the imaginary unit. When the inclusions exhibit viscosity, there exists a phase lag $\delta \in [0, \pi]$ between the stress and strain. This can be expressed by letting λ' and μ' be complex numbers, so that $\arg \lambda' = \arg \mu' = -\delta$.

As shown in Fig. 1, we consider elastic wave scattering in a singly-periodic domain, where the inclusions are arranged periodically in the host matrix along the x_1 direction. We define a unit cell U as $U = (-L/2, L/2) \times \mathbb{R}$ with the

spatial period $L > 0$. In the unit cell U , the host matrix, inclusions, and their boundary are denoted by Ω , $\Omega' = U \setminus \overline{\Omega}$, and Γ , respectively.

When a plane incident wave \mathbf{u}^{in} propagates through the host matrix, the total displacement \mathbf{u} and stress $\boldsymbol{\sigma}$ are governed by the following Navier-Cauchy equations:

$$\sigma_{ji,j}(\mathbf{x}) + \rho\omega^2 u_i(\mathbf{x}) = 0 \quad \mathbf{x} \in \Omega, \quad (1)$$

$$\sigma_{ji,j}(\mathbf{x}) + \rho'\omega^2 u_i(\mathbf{x}) = 0 \quad \mathbf{x} \in \Omega'. \quad (2)$$

We assume that \mathbf{u} and traction \mathbf{t} defined by the unit vector \mathbf{n} outward normal to Ω (inward normal to Ω') are continuous on Γ , i.e.

$$u_i(\mathbf{x}) := u_i|_+(\mathbf{x}) = u_i|_-(\mathbf{x}) \quad \mathbf{x} \in \Gamma, \quad (3)$$

$$t_i(\mathbf{x}) := \sigma_{ji}|_+(\mathbf{x})n_j(\mathbf{x}) = \sigma_{ji}|_-(\mathbf{x})n_j(\mathbf{x}) \quad \mathbf{x} \in \Gamma. \quad (4)$$

Here, we used the Einstein summation convention, and $g|_+$ and $g|_-$ are the traces of a function g defined by

$$g|_{\pm}(\mathbf{x}) = \lim_{h \downarrow 0} g(\mathbf{x} \pm h\mathbf{n}(\mathbf{x})) \quad \mathbf{x} \in \Gamma. \quad (5)$$

The same convention and notation are used throughout the paper. Since \mathbf{u}^{in} is a plane wave, \mathbf{u}^{in} has a quasi-periodicity along the x_1 direction, i.e. there exists a constant $\beta \in (-\pi, \pi]$ such that

$$u_i^{\text{in}}(\mathbf{x} + L\mathbf{e}_1) = u_i^{\text{in}}(\mathbf{x})e^{i\beta}, \quad (6)$$

where $(\mathbf{e}_1, \mathbf{e}_2)$ are the basis vectors of the Cartesian coordinate system (x_1, x_2) . The total displacement \mathbf{u} then satisfies the following quasi-periodic boundary conditions on the left periodic boundary $\Gamma_p = \{\mathbf{x} \mid x_1 = -L/2, x_2 \in \mathbb{R}\}$:

$$u_i(\mathbf{x} + L\mathbf{e}_1) = u_i(\mathbf{x})e^{i\beta}, \quad (7)$$

$$u_{i,1}(\mathbf{x} + L\mathbf{e}_1) = u_{i,1}(\mathbf{x})e^{i\beta}. \quad (8)$$

In summary, the displacement \mathbf{u} is the solution of the following boundary value problem (BVP):

$$\sigma_{ji,j}(\mathbf{x}) + \rho\omega^2 u_i(\mathbf{x}) = 0 \quad \mathbf{x} \in \Omega, \quad (9)$$

$$\sigma_{ji,j}(\mathbf{x}) + \rho'\omega^2 u_i(\mathbf{x}) = 0 \quad \mathbf{x} \in \Omega', \quad (10)$$

$$u_i(\mathbf{x}) = u_i|_+(\mathbf{x}) = u_i|_-(\mathbf{x}) \quad \mathbf{x} \in \Gamma, \quad (11)$$

$$t_i(\mathbf{x}) = \sigma_{ji}|_+(\mathbf{x})n_j(\mathbf{x}) = \sigma_{ji}|_-(\mathbf{x})n_j(\mathbf{x}) \quad \mathbf{x} \in \Gamma, \quad (12)$$

$$u_i(\mathbf{x} + L\mathbf{e}_1) = u_i(\mathbf{x})e^{i\beta} \quad \mathbf{x} \in \Gamma_p, \quad (13)$$

$$u_{i,1}(\mathbf{x} + L\mathbf{e}_1) = u_{i,1}(\mathbf{x})e^{i\beta} \quad \mathbf{x} \in \Gamma_p, \quad (14)$$

Outgoing radiation condition for

$$u_i(\mathbf{x}) - u_i^{\text{in}}(\mathbf{x}) \text{ as } x_2 \rightarrow \pm\infty. \quad (15)$$

2.2 Far-field characteristics

As is known, the solution \mathbf{u} of the periodic scattering problem (9)–(15) admits the following plane-wave expansion:

$$u_i(\mathbf{x}) = \begin{cases} u_i^{\text{in}}(\mathbf{x}) + u_i^{\text{sc},+}(\mathbf{x}) & \mathbf{x} \in U^+ \\ u_i^{\text{in}}(\mathbf{x}) + u_i^{\text{sc},-}(\mathbf{x}) & \mathbf{x} \in U^- \end{cases}, \quad (16)$$

$$\begin{aligned} u_i^{\text{sc},\pm}(\mathbf{x}) &= \sum_{m=-\infty}^{\infty} A^{\text{L}\pm,m} d_i^{\text{L}\pm,m} e^{ik_L \mathbf{x} \cdot \mathbf{p}^{\text{L}\pm,m}} \\ &\quad + \sum_{m=-\infty}^{\infty} A^{\text{T}\pm,m} d_i^{\text{T}\pm,m} e^{ik_T \mathbf{x} \cdot \mathbf{p}^{\text{T}\pm,m}}, \end{aligned} \quad (17)$$

where $U^+ = \{\mathbf{x} \in U \mid x_2 > \max_{y \in \Omega'} y_2\}$ and $U^- = \{\mathbf{x} \in U \mid x_2 < \min_{y \in \Omega'} y_2\}$. Here “L” and “T” represent the longitudinal and transverse waves, respectively, and “ \pm ” represents the directions of the plane waves (+: upward, -: downward). For each index m , called (scattering) channel, the vector $\mathbf{p}^{\text{L}\pm,m}$ denotes the direction of a plane P-wave, which is explicitly written as

$$\mathbf{p}^{\text{L}\pm,m} = \frac{1}{k_L} \left(\frac{\xi_m}{\pm \sqrt{k_L^2 - \xi_m^2}} \right), \quad (18)$$

where $\xi_m = (\beta + 2m\pi)/L$. Throughout the paper, we recognise $\mathbb{C} \ni z \mapsto \sqrt{z}$ by the principal value $\sqrt{z} = \sqrt{|z|} e^{i\frac{1}{2}\text{Arg } z}$, where $\text{Arg} : \mathbb{C} \rightarrow (-\pi, \pi]$ is the principal argument, so that the plane waves do not diverge when radiating into infinity. The direction of motion of the plane P-wave, denoted by $\mathbf{d}^{\text{L}\pm,m}$, is equal to $\mathbf{p}^{\text{L}\pm,m}$. Similarly, the transverse counterparts $\mathbf{p}^{\text{T}\pm,m}$ and $\mathbf{d}^{\text{T}\pm,m}$ are expressed by

$$\mathbf{p}^{\text{T}\pm,m} = \frac{1}{k_T} \left(\frac{\xi_m}{\pm \sqrt{k_T^2 - \xi_m^2}} \right), \quad (19)$$

$$\mathbf{d}^{\text{T}\pm,m} = \frac{1}{k_T} \left(\frac{\pm \sqrt{k_T^2 - \xi_m^2}}{-\xi_m} \right). \quad (20)$$

In what follows, we refer to the plane wave $\mathbf{d}^{\text{L}+,m} e^{ik_L \mathbf{p}^{\text{L}+,m} \cdot \mathbf{x}}$ (resp. $\mathbf{d}^{\text{L}-,m} e^{ik_L \mathbf{p}^{\text{L}-,m} \cdot \mathbf{x}}$) in (17) as an upward (resp. downward) m th plane P-wave. Similarly we use the term “an upward/downward m th plane S-wave.”

Computing the amplitudes $A^{\text{L}\pm,m}$ and $A^{\text{T}\pm,m}$ is the key point of our work. After performing a boundary element analysis, we can compute $A^{\text{L}\pm,m}$ and $A^{\text{T}\pm,m}$ using the following boundary integrals (see Appendix A):

$$\begin{aligned} A^{\text{L}\pm,m} &= \frac{i}{2L(\lambda + 2\mu)\sqrt{k_L^2 - \xi_m^2}} \int_{\Gamma} \left[d_i^{\text{L}\pm,m} \sigma_{ji}(\mathbf{x}) \right. \\ &\quad \left. + ik_L \left(\lambda \delta_{ij} + 2\mu p_i^{\text{L}\pm,m} p_j^{\text{L}\pm,m} \right) u_i(\mathbf{x}) \right] \\ &\quad \times n_j(\mathbf{x}) e^{-ik_L \mathbf{x} \cdot \mathbf{p}^{\text{L}\pm,m}} d\Gamma, \end{aligned} \quad (21)$$

$$\begin{aligned} A^{\text{T}\pm,m} &= \frac{i}{2L\mu\sqrt{k_T^2 - \xi_m^2}} \int_{\Gamma} \left[d_i^{\text{T}\pm,m} \sigma_{ji}(\mathbf{x}) \right. \\ &\quad \left. + ik_T \mu \left(p_i^{\text{T}\pm,m} d_j^{\text{T}\pm,m} + d_i^{\text{T}\pm,m} p_j^{\text{T}\pm,m} \right) u_i(\mathbf{x}) \right] \\ &\quad \times n_j(\mathbf{x}) e^{-ik_T \mathbf{x} \cdot \mathbf{p}^{\text{T}\pm,m}} d\Gamma, \end{aligned} \quad (22)$$

where δ_{ij} is the Kronecker delta. Note that the displacement fields in U^+ and U^- are completely determined from the plane-wave expansion (17) and boundary integrals of the solution (21) and (22). Moreover, the plane wave expansion (17) includes the propagating modes and evanescent modes, the latter of which can be neglected in far fields owing to their exponential decay. We therefore define the index sets $I_L = \{m \in \mathbb{Z} \mid k_L^2 - \xi_m^2 > 0\}$ and $I_T = \{m \in \mathbb{Z} \mid k_T^2 - \xi_m^2 > 0\}$, so that the scattered waves $u^{sc,\pm}$ are approximated in the far fields as

$$\begin{aligned} u^{sc,\pm}(\mathbf{x}) \simeq & \sum_{m \in I_L} A^{L\pm,m} d_i^{L\pm,m} e^{ik_L \mathbf{x} \cdot \mathbf{p}^{L\pm,m}} \\ & + \sum_{m \in I_T} A^{T\pm,m} d_i^{T\pm,m} e^{ik_T \mathbf{x} \cdot \mathbf{p}^{T\pm,m}} \end{aligned} \quad \text{as } |x_2| \rightarrow \infty. \quad (23)$$

This representation of far-field behaviour allows us to define reflectance and transmittance in a natural manner. From (17) and the orthogonality of the exponential function, it can be seen that the time-averaged energy E^\pm per unit cell radiating when x_2 tends to the infinities $\pm\infty$ equals the sum of the energy carried by the propagating plane waves, i.e.

$$\begin{aligned} E^\pm = & \frac{\omega L}{2} \sum_{m \in I_L} |A^{L\pm,m}|^2 (\lambda + 2\mu) \sqrt{k_L^2 - \xi_m^2} \\ & + \frac{\omega L}{2} \sum_{m \in I_T} |A^{T\pm,m}|^2 \mu \sqrt{k_T^2 - \xi_m^2}. \end{aligned} \quad (24)$$

In addition, if the system has viscosity, i.e. $\text{Im}[\lambda'] < 0$ and $\text{Im}[\mu'] < 0$, then the time-averaged amount of energy loss per unit cell is

$$E^{\text{loss}} = \frac{\omega}{2} \text{Im} \left[\int_{\Gamma} \sigma_{ij}(\mathbf{x}) \bar{u}_j(\mathbf{x}) n_i(\mathbf{x}) d\Gamma \right] \geq 0. \quad (25)$$

According to the energy conservation law, the time-averaged incident energy E^{in} per unit cell should be equal to the sum of E^+ , E^- , and E^{loss} . Therefore, if the incident wave propagates upwards, then we define the transmittance T of an incident wave by $T = E^+ / E^{\text{in}}$ and reflectance R by $R = E^- / E^{\text{in}}$; otherwise $T = E^- / E^{\text{in}}$ and $R = E^+ / E^{\text{in}}$.

3 Topology optimisation

3.1 Objective functional

Our objective is to design the shape and topology of an elastic metamaterial slab that achieves some novel functionalities. As mentioned in Section 2.2, some important properties including the energy balance and far-field behaviour are given by the boundary integrals of the form

$$\int_{\Gamma} (\phi_{ij}(\mathbf{x}) u_i(\mathbf{x}) + \psi_i(\mathbf{x}) \sigma_{ij}(\mathbf{x})) n_j(\mathbf{x}) d\Gamma, \quad (26)$$

where ϕ and ψ are differentiable symmetric-tensor- and vector-valued functions, respectively. Here we focus on the objective functionals of this form (26) and derive a corresponding design sensitivity.

3.2 Level-set based algorithm for topology optimisation

In this study, we adopt a level-set-based algorithm for our topology optimisation. Our algorithm essentially follows the method proposed by Amstutz and André [25] and assumes that a level set function ϕ defined in a bounded and fixed design domain D is governed by

$$\frac{\partial \phi}{\partial t}(\mathbf{x}, t) = \mathcal{T}(\mathbf{x}, t) - (\mathcal{T}, \phi)_{L^2(D)}\phi(\mathbf{x}, t), \quad (27)$$

where \mathcal{T} is the topological derivative of an objective functional (discussed in the next subsection), and $(\cdot, \cdot)_{L^2(D)}$ is the L^2 inner product in D defined by

$$(f, g)_{L^2(D)} = \int_D f(\mathbf{x})g(\mathbf{x})d\Omega. \quad (28)$$

The equation (27) guarantees that the obtained design satisfies an optimality condition in terms of a topological perturbation once ϕ converges [29]. However, this method cannot control the complexity of a designed structure, which is essential for engineering applications. Thus, we employ an approach that uses B-spline basis functions for interpolating ϕ and \mathcal{T} in space [26]. This allows us to limit the ratio of the perimeter and area of the structure by changing the number or degree of the B-spline basis functions.

3.3 Topological derivative

As mentioned in the previous subsection, we consider complex-valued functions of the form

$$\begin{aligned} f(\mathbf{u}(\Omega), \boldsymbol{\sigma}(\Omega), \phi, \psi; \Gamma) \\ = \int_{\Gamma} (\phi_{ij}(\mathbf{x})u_i(\mathbf{x}) + \psi_i(\mathbf{x})\sigma_{ij}(\mathbf{x}))n_j(\mathbf{x})d\Gamma. \end{aligned} \quad (29)$$

Here we assume that ϕ and ψ are independent of Ω for simplicity. We note that removing this assumption is trivial.

Let $(\mathbf{u}(\Omega), \boldsymbol{\sigma}(\Omega))$ be the solution of the BVP (9)–(15) and assume that f can be expanded as

$$\begin{aligned} & f(\mathbf{u}(\Omega \setminus \bar{\Omega}_{\varepsilon}), \boldsymbol{\sigma}(\Omega \setminus \bar{\Omega}_{\varepsilon}), \phi, \psi; \partial(\Omega \setminus \bar{\Omega}_{\varepsilon})) \\ &= f(\mathbf{u}(\Omega), \boldsymbol{\sigma}(\Omega), \phi, \psi; \Gamma) + v(\varepsilon)\mathcal{T}(\mathbf{x}^0) + o(v(\varepsilon)) \\ & \quad \mathbf{x}^0 \in \Omega, \end{aligned} \quad (30)$$

$$\begin{aligned} & f(\mathbf{u}(\Omega \cup \Omega_{\varepsilon}), \boldsymbol{\sigma}(\Omega \cup \Omega_{\varepsilon}), \phi, \psi; \Gamma \cup \partial\Omega_{\varepsilon}) \\ &= f(\mathbf{u}(\Omega), \boldsymbol{\sigma}(\Omega), \phi, \psi; \Gamma) + v(\varepsilon)\mathcal{T}(\mathbf{x}^0) + o(v(\varepsilon)) \\ & \quad \mathbf{x}^0 \in \Omega', \end{aligned} \quad (31)$$

where v is a monotonically decreasing function which vanishes when ε tends to zero, and $\Omega_{\varepsilon} = B_{\varepsilon}(\mathbf{x}^0)$ is a disk of radius $\varepsilon > 0$ centred at \mathbf{x}^0 . The function \mathcal{T} is called a *topological derivative* [27].

Here we focus on the case of $\mathbf{x}^0 \in \Omega$ because the other case can be treated in a similar manner. We define $\delta\mathbf{u} = \mathbf{u}(\Omega \setminus \bar{\Omega}_{\varepsilon}) - \mathbf{u}(\Omega)$ and $\delta\boldsymbol{\sigma} = \boldsymbol{\sigma}(\Omega \setminus \bar{\Omega}_{\varepsilon}) - \boldsymbol{\sigma}(\Omega)$

and omit the argument of $\mathbf{u}(\Omega)$ and $\boldsymbol{\sigma}(\Omega)$ for ease of notation. Then we can write

$$\begin{aligned}\delta f &= f(\mathbf{u}(\Omega \setminus \bar{\Omega}_\varepsilon), \boldsymbol{\sigma}(\Omega \setminus \bar{\Omega}_\varepsilon), \phi, \psi; \partial(\Omega \setminus \bar{\Omega}_\varepsilon)) \\ &\quad - f(\mathbf{u}(\Omega), \boldsymbol{\sigma}(\Omega), \phi, \psi; \Gamma) \\ &= f(\mathbf{u} + \delta\mathbf{u}, \boldsymbol{\sigma} + \delta\boldsymbol{\sigma}, \phi, \psi; \Gamma \cup \partial\Omega_\varepsilon) \\ &\quad - f(\mathbf{u}, \boldsymbol{\sigma}, \phi, \psi; \Gamma) \\ &= f(\mathbf{u}, \boldsymbol{\sigma}, \phi, \psi; \partial\Omega_\varepsilon) + f(\delta\mathbf{u}, \delta\boldsymbol{\sigma}, \phi, \psi; \Gamma) \\ &\quad + f(\delta\mathbf{u}, \delta\boldsymbol{\sigma}, \phi, \psi; \partial\Omega_\varepsilon).\end{aligned}\tag{32}$$

The first term in (32) is easily evaluated by the Gauss theorem and written as

$$\begin{aligned}f(\mathbf{u}, \boldsymbol{\sigma}, \phi, \psi; \partial\Omega_\varepsilon) &= \pi\varepsilon^2 \left[(-\phi_{ij}(\mathbf{x}^0) D_{ijkl} - \psi_{k,l}(\mathbf{x}^0)) \sigma_{kl}(\mathbf{x}^0) \right. \\ &\quad \left. + (\rho\omega^2 \psi_i(\mathbf{x}^0) - \phi_{ij,j}(\mathbf{x}^0)) u_i(\mathbf{x}^0) \right] + O(\varepsilon^3),\end{aligned}\tag{33}$$

where \mathbf{D} is the compliance tensor given by

$$D_{ijkl} = \frac{1}{4\mu} \left(-\frac{\lambda}{\lambda + \mu} \delta_{ij} \delta_{kl} + \delta_{ik} \delta_{jl} + \delta_{il} \delta_{jk} \right).\tag{34}$$

To evaluate the second term in (32) using the adjoint variable method, we derive a reciprocal relation for the quasi-periodic problem. Let \mathbf{u}^1 be a solution of

$$\sigma_{ij}^1(\mathbf{x}) + \rho\omega^2 u_i^1(\mathbf{x}) = 0 \quad \mathbf{x} \in \Omega,\tag{35}$$

$$u_i^1(\mathbf{x} + L\mathbf{e}_1) = u_i^1(\mathbf{x}) e^{i\beta} \quad \mathbf{x} \in \Gamma_p,\tag{36}$$

$$u_{i,1}^1(\mathbf{x} + L\mathbf{e}_1) = u_{i,1}^1(\mathbf{x}) e^{i\beta} \quad \mathbf{x} \in \Gamma_p,\tag{37}$$

$$\text{Outgoing radiation condition for } u_i^1(\mathbf{x}) \text{ as } |\mathbf{x}| \rightarrow \infty,\tag{38}$$

and let \mathbf{u}^2 be a solution of

$$\sigma_{ij}^2(\mathbf{x}) + \rho\omega^2 u_i^2(\mathbf{x}) = 0 \quad \mathbf{x} \in \Omega,\tag{39}$$

$$u_i^2(\mathbf{x} + L\mathbf{e}_1) = u_i^2(\mathbf{x}) e^{-i\beta} \quad \mathbf{x} \in \Gamma_p,\tag{40}$$

$$u_{i,1}^2(\mathbf{x} + L\mathbf{e}_1) = u_{i,1}^2(\mathbf{x}) e^{-i\beta} \quad \mathbf{x} \in \Gamma_p,\tag{41}$$

$$\text{Outgoing radiation condition for } u_i^2(\mathbf{x}) \text{ as } |\mathbf{x}| \rightarrow \infty,\tag{42}$$

where $\sigma_{ij}^1 = C_{ijkl} u_{k,l}^1$ and $\sigma_{ij}^2 = C_{ijkl} u_{k,l}^2$ (Note that the superscripted indices here do not indicate exponential). Using the quasi-periodic conditions, outgoing radiation condition, and Betti's reciprocal theorem, we see that the following reciprocal relation holds:

$$\int_{\Gamma} (\sigma_{ji}^1 u_i^2 - \sigma_{ji}^2 u_i^1) n_j d\Gamma = 0.\tag{43}$$

Note that not only the same radiation condition but also the quasi-periodic conditions with the phase differences of opposite sign are required.

Now we define an adjoint variable $(\tilde{\mathbf{u}}, \tilde{\boldsymbol{\sigma}})$ which satisfies

$$\tilde{\sigma}_{ij}(\mathbf{x}) + \rho\omega^2\tilde{u}_i(\mathbf{x}) = 0 \quad \mathbf{x} \in \Omega, \quad (44)$$

$$\tilde{\sigma}'_{ij}(\mathbf{x}) + \rho'\omega^2\tilde{u}_i(\mathbf{x}) = 0 \quad \mathbf{x} \in \Omega', \quad (45)$$

$$\tilde{u}_i(\mathbf{x}) := \tilde{u}_i|_+(\mathbf{x}) = \tilde{u}_i|_-(\mathbf{x}) - \psi_i(\mathbf{x}) \quad \mathbf{x} \in \Gamma, \quad (46)$$

$$\tilde{\sigma}_{ji}|_+(\mathbf{x})n_j(\mathbf{x}) = \tilde{\sigma}_{ji}|_-(\mathbf{x})n_j(\mathbf{x}) + \phi_{ji}(\mathbf{x})n_j(\mathbf{x}) \quad \mathbf{x} \in \Gamma, \quad (47)$$

$$\tilde{u}_i(\mathbf{x} + L\mathbf{e}_1) = \tilde{u}_i(\mathbf{x})e^{-i\beta} \quad \mathbf{x} \in \Gamma_p, \quad (48)$$

$$\tilde{u}_{i,1}(\mathbf{x} + L\mathbf{e}_1) = \tilde{u}_{i,1}(\mathbf{x})e^{-i\beta} \quad \mathbf{x} \in \Gamma_p, \quad (49)$$

$$\text{Outgoing radiation condition for } \tilde{u}_i(\mathbf{x}) \text{ as } x_2 \rightarrow \pm\infty, \quad (50)$$

and

$$\tilde{\sigma}_{ij}(\mathbf{x}) = \begin{cases} C_{ijkl}u_{k,l}(\mathbf{x}) & \mathbf{x} \in \Omega \\ C'_{ijkl}u_{k,l}(\mathbf{x}) & \mathbf{x} \in \Omega' \end{cases}. \quad (51)$$

Then the reciprocal relation (43) and the Betti's reciprocal theorem for bounded domains yield

$$f(\delta\mathbf{u}, \delta\boldsymbol{\sigma}, \boldsymbol{\phi}, \boldsymbol{\psi}; \Gamma) = -f(\delta\mathbf{u}, \delta\boldsymbol{\sigma}, \tilde{\boldsymbol{\sigma}}, -\tilde{\mathbf{u}}; \partial\Omega_\varepsilon). \quad (52)$$

Now the second and third terms in (32) are written by the integrals around Ω_ε . From the result of [28], the perturbed solutions admit the following expansions:

$$u_i(\mathbf{x}) + \delta u_i(\mathbf{x}) = u_i(\mathbf{x}^0) + O(\varepsilon) \quad \mathbf{x} \in \Omega_\varepsilon, \quad (53)$$

$$\sigma_{ij}(\mathbf{x}) + \delta\sigma_{ij}(\mathbf{x}) = A_{ijkl}\sigma_{kl}(\mathbf{x}^0) + O(\varepsilon) \quad \mathbf{x} \in \Omega_\varepsilon, \quad (54)$$

where \mathbf{A} is the fourth-order tensor given by the elastic tensors

$$C_{ijkl} = \lambda\delta_{ij}\delta_{kl} + \mu(\delta_{ik}\delta_{jl} + \delta_{il}\delta_{jk}), \quad (55)$$

$$C'_{ijkl} = \lambda'\delta_{ij}\delta_{kl} + \mu'(\delta_{ik}\delta_{jl} + \delta_{il}\delta_{jk}), \quad (56)$$

Eshelby's tensor [30]

$$\begin{aligned} S_{ijkl} = & \frac{1}{4(\lambda+2\mu)} [(\lambda-\mu)\delta_{ij}\delta_{kl} \\ & + (\lambda+3\mu)(\delta_{ik}\delta_{jl} + \delta_{il}\delta_{jk})], \end{aligned} \quad (57)$$

and identity tensor $I_{ijkl} = \frac{1}{2}(\delta_{ik}\delta_{jl} + \delta_{il}\delta_{jk})$ as

$$\mathbf{A} = \mathbf{C}' : (\mathbf{I} + \mathbf{S} : (\mathbf{C}' - \mathbf{C}) : \mathbf{D})^{-1} : \mathbf{D}, \quad (58)$$

with the inverse \mathbf{X}^{-1} of a symmetric fourth order tensor $X_{ijkl} = a\delta_{ij}\delta_{kl} + b(\delta_{ik}\delta_{jl} + \delta_{il}\delta_{jk})$ given by

$$(\mathbf{X}^{-1})_{ijkl} = -\frac{a}{4b(a+b)}\delta_{ij}\delta_{kl} + \frac{1}{4b}(\delta_{ik}\delta_{jl} + \delta_{il}\delta_{jk}), \quad (59)$$

and the double inner product $(\mathbf{X} : \mathbf{Y})_{ijkl} = X_{ijmn}Y_{mnkl}$ between X_{ijkl} and $Y_{ijkl} = c\delta_{ij}\delta_{kl} + d(\delta_{ik}\delta_{jl} + \delta_{il}\delta_{jk})$, computed by

$$(\mathbf{X} : \mathbf{Y})_{ijkl} = 2(ac + ad + bc)\delta_{ij}\delta_{kl} + 2bd(\delta_{ik}\delta_{jl} + \delta_{il}\delta_{jk}). \quad (60)$$

The asymptotic expansions (53) and (54) yield

$$\begin{aligned}
& f(\delta \mathbf{u}, \delta \boldsymbol{\sigma}, \phi, \psi; \partial \Omega_\varepsilon) \\
&= \pi \varepsilon^2 \left[(\phi_{kl}(\mathbf{x}^0) D_{klmn} + \psi_{m,n}(\mathbf{x}^0) - \phi_{ij}(\mathbf{x}^0) D'_{ijkl} A_{klmn} \right. \\
&\quad \left. - \psi_{k,l}(\mathbf{x}^0) A_{klmn}) \sigma_{mn}(\mathbf{x}^0) + (\rho' - \rho) \omega^2 \psi_i(\mathbf{x}^0) u_i(\mathbf{x}^0) \right] \\
&\quad + O(\varepsilon^3), \tag{61}
\end{aligned}$$

where $\mathbf{D}' = (\mathbf{C}')^{-1}$. From (33) and (61) along with (52), we finally arrive at

$$\begin{aligned}
\delta f = & \pi \varepsilon^2 \left[\tilde{\sigma}_{ij}(\mathbf{x}^0) (D'_{ijkl} - D_{ijkl}) A_{klmn} \sigma_{mn}(\mathbf{x}^0) \right. \\
& + (\rho' - \rho) \omega^2 \tilde{u}_i(\mathbf{x}^0) u_i(\mathbf{x}^0) \\
& + \left(-\phi_{ij}(\mathbf{x}^0) D'_{ijkl} - \frac{\psi_{k,l}(\mathbf{x}^0) + \psi_{l,k}(\mathbf{x}^0)}{2} \right) \\
& \times A_{klmn} \sigma_{mn}(\mathbf{x}^0) \\
& \left. + (-\phi_{ij,j}(\mathbf{x}^0) + \rho' \omega^2 \psi_i(\mathbf{x}^0)) u_i(\mathbf{x}^0) \right] + O(\varepsilon^3), \tag{62}
\end{aligned}$$

which gives the topological derivative

$$\begin{aligned}
\mathcal{T}(\mathbf{x}) = & \tilde{\sigma}_{ij}(\mathbf{x}^0) (D'_{ijkl} - D_{ijkl}) A_{klmn} \sigma_{mn}(\mathbf{x}^0) \\
& + (\rho' - \rho) \omega^2 \tilde{u}_i(\mathbf{x}^0) u_i(\mathbf{x}^0) \\
& + \left(-\phi_{ij}(\mathbf{x}^0) D'_{ijkl} - \frac{\psi_{k,l}(\mathbf{x}^0) + \psi_{l,k}(\mathbf{x}^0)}{2} \right) \\
& \times A_{klmn} \sigma_{mn}(\mathbf{x}^0) \\
& + (-\phi_{ij,j}(\mathbf{x}^0) + \rho' \omega^2 \psi_i(\mathbf{x}^0)) u_i(\mathbf{x}^0) \quad \mathbf{x} \in \Omega. \tag{63}
\end{aligned}$$

Similarly, we conclude that the topological derivative in Ω' is given by

$$\begin{aligned}
\mathcal{T}(\mathbf{x}) = & \tilde{\sigma}_{ij}(\mathbf{x}^0) (D_{ijkl} - D'_{ijkl}) A'_{klmn} \sigma_{mn}(\mathbf{x}^0) \\
& + (\rho - \rho') \omega^2 \tilde{u}_i(\mathbf{x}^0) u_i(\mathbf{x}^0) \\
& + \left(-\phi_{ij}(\mathbf{x}^0) D_{ijkl} - \frac{\psi_{k,l}(\mathbf{x}^0) + \psi_{l,k}(\mathbf{x}^0)}{2} \right) \\
& \times A'_{klmn} \sigma_{mn}(\mathbf{x}^0) \\
& + (-\phi_{ij,j}(\mathbf{x}^0) + \rho \omega^2 \psi_i(\mathbf{x}^0)) u_i(\mathbf{x}^0) \quad \mathbf{x} \in \Omega', \tag{64}
\end{aligned}$$

where \mathbf{A}' is obtained by interchanging (λ, μ) and (λ', μ') in \mathbf{A} . The direct problem (9)–(15) and adjoint problem (44)–(50) are numerically solved by the boundary element method to obtain \mathbf{u} , $\boldsymbol{\sigma}$, $\tilde{\mathbf{u}}$, and $\tilde{\boldsymbol{\sigma}}$ (see Appendix B).

4 Numerical examples

Here we demonstrate some examples of our topology optimisation.

4.1 Elastic wave absorber

First we explore an optimal configuration that maximises the amount of energy absorbed by viscoelastic inclusions embedded in a perfectly-elastic host medium, which is called an elastic wave absorber. To this end, the objective functional J to be maximised is chosen as the loss ratio

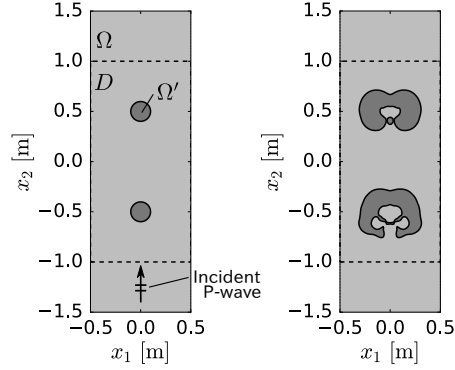
$$J = \frac{1}{E^{\text{in}}} \text{Im} \left[\int_{\Gamma} \sigma_{ij}(\mathbf{x}) \bar{u}_i(\mathbf{x}) n_j(\mathbf{x}) d\Gamma \right], \quad (65)$$

whose maximum value 1 is attained if and only if the system absorbs all the incident energy.

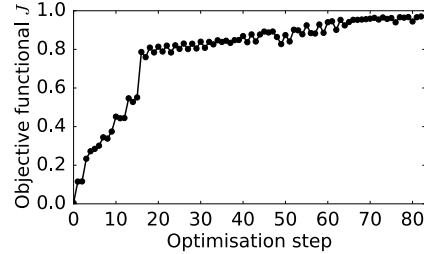
As shown in Fig. 2 (a), we defined a fixed design domain D as the rectangular region $D = (-0.5 \text{ m}, 0.5 \text{ m}) \times (-1.0 \text{ m}, 1.0 \text{ m})$. The geometrical periodicity L is fixed at $L = 1 \text{ m}$ throughout the topology optimisation. In this example, the host matrix Ω and viscoelastic inclusion Ω' are assumed to be steel (mass density $7.80 \times 10^3 \text{ kg/m}^3$, Young's modulus 205 GPa, and Poisson's ratio 0.30) and epoxy resin (mass density $1.85 \times 10^3 \text{ kg/m}^3$, Young's modulus 3.00 GPa, Poisson's ratio 0.34, and phase lag 10 deg), respectively. A plane P-wave with a frequency of 1.8 kHz is given in the upward direction perpendicular to the array. Here the initial configuration shown in Fig. 2 (a) consists of two layers of circular inclusions, but this choice is not necessarily the best and may affect the performance of our topology optimisation. From Fig. 2 (c), we see that the upper bound of J is almost realised at the 82th step (final step). This can be observed from Fig. 2 (d) and (e) as well. For the initial configuration, we can see little interference around the inclusions; consequently, the incident wave is passing through the absorber with almost no reflection or absorption. Conversely, the optimised configuration exhibits strong interference in the structure, resulting in efficient energy absorption.

Although our topology optimisation does not consider the robustness to frequency perturbation, we are interested in whether the designed absorber can maintain such a high performance when the frequency varies from the target value of $f = 1.8 \text{ kHz}$. To analyse the performance, we compare the designed absorber (Fig. 2 (b)) and viscoelastic slab, which is obtained by filling the same viscoelastic material in D . From Fig. 3, we observe that the designed absorber attains the maximum loss ratio around the target frequency 1.8 kHz and exhibits degradation in performance as the frequency moves away from the target value. However, the viscoelastic slab absorbs almost 20% of the incident energy within the spectrum, which is substantially less than that by the designed absorber. These results indicate that the designed absorber performs well even in a wide range of spectrum compared with conventional structures.

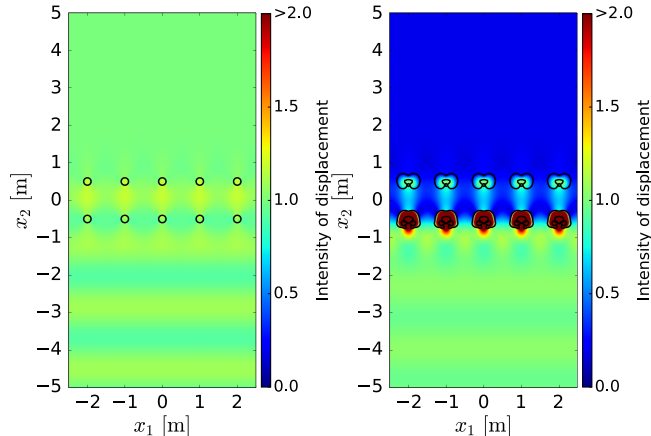
Although the designed structure achieves wideband performance, better spectral properties can be expected by stacking the slab in the x_2 direction and increasing the thickness of the absorber. Here we regard the fixed design domain D as a unit cell of the layered structure and perform the same topology optimisation to design a triple-layered absorber as shown in Fig. 4. Furthermore, we performed a spectral analysis and plotted the results in Fig. 3. We can see that the designed absorber has a different shape and performs slightly better than the original absorber in the frequency range 1.4–2.2 kHz.



(a) Initial configuration (b) Optimised configuration



(c) History of J



(d) Displacement in the initial configuration (e) Displacement in the optimised configuration

Figure 2: Result of the topology optimisation of the elastic wave absorber. (a) and (b) show the initial and optimised configurations, respectively. (c) illustrates the history of the objective functional J in the optimisation procedure. Also, (d) and (e) show the intensity of displacement (time-averaged amplitude of the displacement normalised by that of the incident wave) in the initial and optimised configurations, respectively

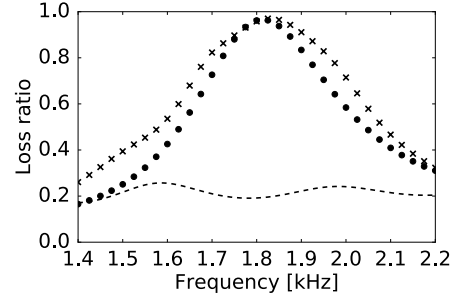


Figure 3: Loss ratio for the designed elastic wave absorber (circular dots), viscoelastic slab (dashed line), and triple-layered elastic wave absorber shown in Fig. 4 (b) (discrete crosses).

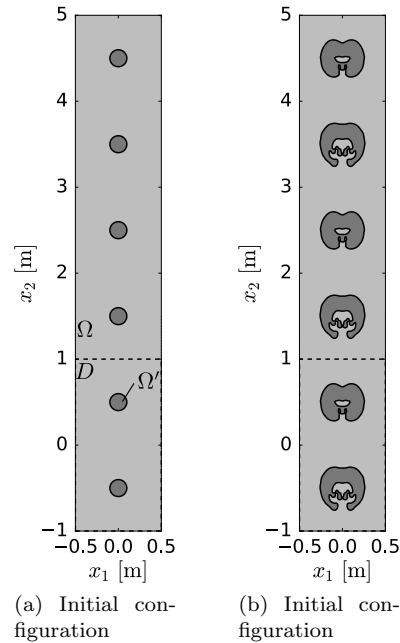


Figure 4: Result of the topology optimisation of the triple-layered elastic wave absorber.

4.2 Wave-mode converter

Our elastic metamaterial slabs would achieve another interesting functionality. We recall the far-field characteristics (23) and see that the scattered S-waves can be excited with only a plane P-wave, and vice versa. This implies that it would be possible to realise a metamaterial slab which converts an incident P-wave (resp. S-wave) into transmitted S-waves (resp. P-waves). We term this metamaterial slab a wave-mode converter.

Here, we focus on the ‘P-wave to S-wave’ conversion. To realise this wave-mode conversion, we define the objective function J so that a transmitted wave is composed of only plane S-waves when J attains its minimum value -1 if and only if the amplitudes of transmitted P-waves $A^{L+,m}$, reflected P-waves $A^{L-,m}$, and reflected S-waves $A^{T-,m}$ are minimised, and the amplitudes of transmitted S-waves $A^{T+,m}$ are maximised, i.e. we minimise

$$J = \frac{\omega^2 L \sqrt{\rho}}{2E^{\text{in}}} \left[\sum_{m \in I_L} \sqrt{\lambda + 2\mu} \times \left(|p_2^{L+,m}| |A^{L+,m}|^2 + |p_2^{L-,m}| |A^{L-,m}|^2 \right) - \sum_{m \in I_T} \sqrt{\mu} \left(|p_2^{T+,m}| |A^{T+,m}|^2 - |p_2^{T-,m}| |A^{T-,m}|^2 \right) \right]. \quad (66)$$

We demonstrate a numerical example of topology optimisation of the wave-mode converter. In this example, we use the same material constants as the previous optimisation; however, the phase lag δ in Ω' is changed to 0 so that the inclusion is perfectly elastic.

We give an incident plane P-wave propagating in the upward direction perpendicular to the array, which is periodic along the x_1 direction with $L = 1.0$ m as shown in Fig. 5 (a). The frequency is set to 3.8 kHz. In this setting, we have one P-wave channel $I_L = \{0\}$ and three S-wave channels $I_T = \{-1, 0, 1\}$. Note that the number of the channels and the direction of each channel are independent of the shape of the inclusions.

Fig. 5 (b) illustrates the optimised configuration, and Fig. 5 (c) shows the history of the value of J for each optimisation step. As with the previous optimisation, we have almost reached the lower bound $J = -1$ at the 64th step (final step). This means that the optimised structure converts the incident P-wave into S-waves propagating through the upward -1 th and 1 th S-wave channels. We can confirm this from Fig. 5 (d) and (e), where we have computed the amplitudes of each plane wave in the far fields by numerically evaluating the integrals (21) and (22). For the initial configuration, we can observe almost no reflection or excitation of the S-waves whereas the optimised configuration diffracts the incident wave in the oblique directions. In addition, we have plotted the displacement field in Fig. 6, from which we confirm that the divergence vanishes within the top of the slab and transmitted wave has only rotational components.

4.3 Negative refraction

We finally show that our metamaterial slab can exhibit negative refraction, i.e. a transmitted wave propagates in an opposite horizontal direction to an incident

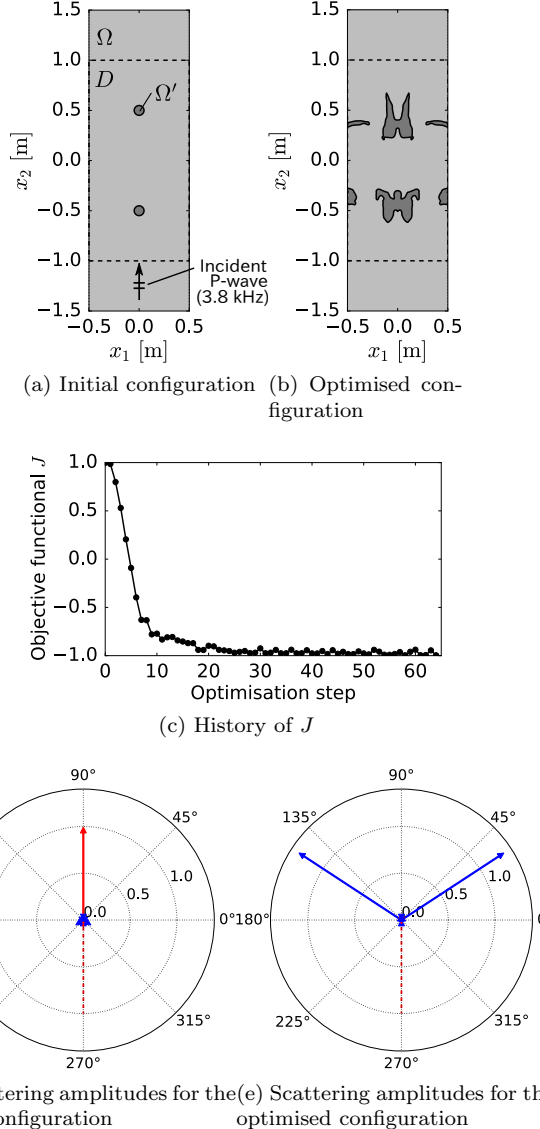


Figure 5: Result of the topology optimisation of the wave-mode converter. (a) and (b) show the initial and optimised configurations, respectively. (c) illustrates the history of the objective functional J in the optimisation procedure. In (d) and (e), the red and blue arrows respectively denote the directions and magnitudes of the scattered P- and S-waves in the far fields. The directions of the arrows denote their directions of propagation $p^{L\pm,m}$ or $p^{T\pm,m}$, and the length represents their amplitudes $|A^{L\pm,m}|$ or $|A^{T\pm,m}|$ for each propagating channel m . The magnitudes are normalised by that of the incident wave. In addition, the red dashed lines indicate the incident P-wave

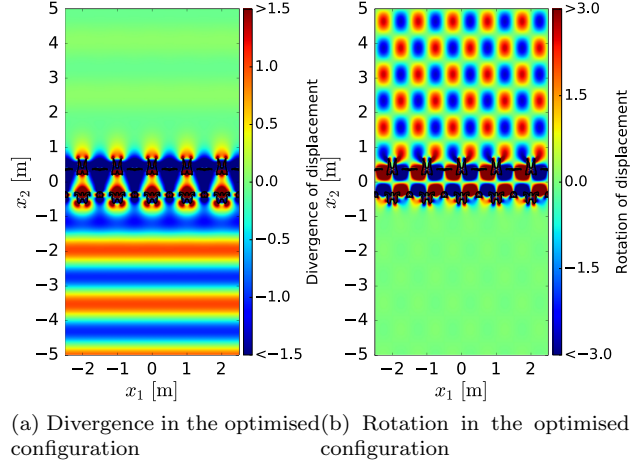


Figure 6: Displacement field at $t = 0$ around the designed wave-mode converter (Fig. 5 (b)). (a) and (b) show the divergence and rotation of the total displacement field normalised by the amplitude of the incident wave, respectively

wave. We consider the negative refraction of a P-wave. Similar to (66), we define the objective functional J as

$$\begin{aligned}
J = & \frac{\omega^2 L \sqrt{\rho}}{2E^{\text{in}}} \left[\sum_{m \in I_L} \sqrt{\mu} \right. \\
& \times \left(|p_2^{\text{T},m}| |A^{\text{T},m}|^2 + |p_2^{\text{T},-m}| |A^{\text{T},-m}|^2 \right) \\
& + \sum_{m \in I_L \setminus \{-1\}} \sqrt{\lambda + 2\mu} |p_2^{\text{L},m}| |A^{\text{L},m}|^2 \\
& + \sum_{m \in I_L} \sqrt{\lambda + 2\mu} |p_2^{\text{L},-m}| |A^{\text{L},-m}|^2 \\
& \left. - \sqrt{\lambda + 2\mu} |p_2^{\text{L},-1}| |A^{\text{L},-1}|^2 \right], \quad (67)
\end{aligned}$$

so that the slab diffracts an incident P-wave in the upward -1 th P-wave channel without any reflection. Note that this objective function is not valid for a low frequency range because we assume $-1 \in I_L$, which is equivalent to $k_L > \pi/L$.

We used the same material constants and initial configuration as the previous optimisation and give an incident plane P-wave with a frequency of 4.8 kHz and incident angle of 30 deg as shown in Fig. 7 (a). Then the channel indices are $I_L = \{-1, 0\}$ and $I_T = \{-1, 0, 1\}$.

We illustrated the optimised configuration in Fig. 7 (b) and the history of J in Fig. 7 (c). Different from the previous two optimisations, the lower bound $J = -1$ is not perfectly attained; however we can observe the negative refraction from Fig. 7 (e) and Fig. 8 while Fig. 7 (d) indicate very weak scattering. We note that our topology optimisation is slightly sensitive to the initial configuration; therefore a possibility that we can find a better solution exists.

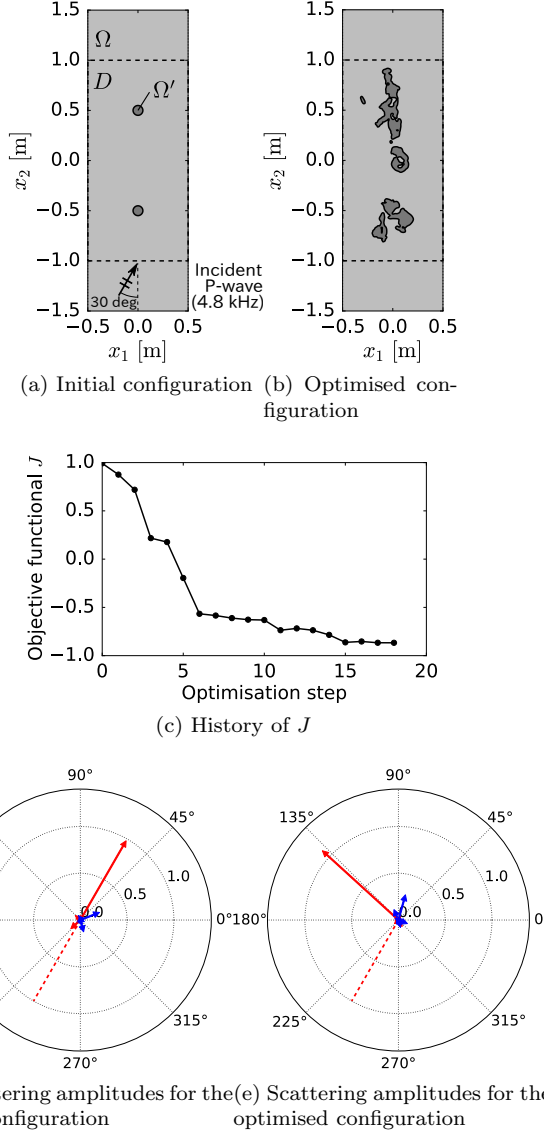
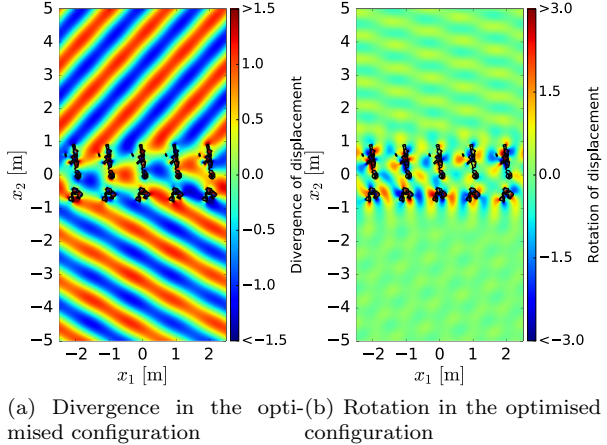


Figure 7: Result of the topology optimisation of the wave-mode converter. (a) and (b) show the initial and optimised configurations, respectively. (c) illustrates the history of the objective functional J in the optimisation procedure. In (d) and (e), the red and blue arrows denote respectively the directions and magnitudes of the scattered P- and S-waves in the far fields. The directions of the arrows denote their directions of propagation $p^{L\pm,m}$ or $p^{T\pm,m}$, and the length represents their amplitudes $|A^{L\pm,m}|$ or $|A^{T\pm,m}|$ for each propagating channel m . The magnitudes are normalised by that of the incident wave. In addition, the red dashed lines indicate the incident P-wave



(a) Divergence in the opti-(b) Rotation in the optimised
mised configuration configuration

Figure 8: Displacement field at $t = 0$ around the designed metamaterial slab (Fig. 7 (b)). (a) and (b) show the divergence and rotation of the total displacement field normalised by the amplitude of the incident wave, respectively

5 Conclusion

This paper presented a numerical method for a topology optimisation of elastic metamaterial slabs. Our proposed method is based on a new objective functional that describes the far-field behaviour of scattering waves. The corresponding topological derivative is derived and incorporated into a level-set-based topology optimisation algorithm. Through numerical examples, we confirmed that our topology optimisation successfully designs metamaterials that exhibit perfect absorption, wave-mode conversion, and negative refraction.

Our topology optimisation does not consider the robustness to perturbation of frequencies or incident angles. From a practical perspective, it must be ensured that the designed material possesses desired robustness, which we will study in our future works.

A Periodic Green's function and far-field characteristics

A.1 Periodic Green's function

To analyse the periodic scattering problem (9)–(15), we first consider Green's function G_{ij}^P satisfying

$$(\lambda + \mu)G_{kj,ik}^P(\mathbf{x}, \mathbf{y}) + \mu G_{ij,kk}^P(\mathbf{x}, \mathbf{y}) + \rho\omega^2 G_{ij}^P(\mathbf{x}, \mathbf{y}) = -\delta(\mathbf{x} - \mathbf{y})\delta_{ij}, \quad (68)$$

$$G_{ij}^P(\mathbf{x} + L\mathbf{e}_1, \mathbf{y}) = G_{ij}^P(\mathbf{x}, \mathbf{y})e^{i\beta}, \quad (69)$$

and the radiation condition, where δ_{ij} is the Kronecker delta, and $\delta(\mathbf{x})$ is the Dirac delta function. This Green's function G_{ij}^P is called *periodic Green's function*.

tion and known to have the following representation:

$$G_{ij}^p(\mathbf{x}, \mathbf{y}) = \sum_{n=-\infty}^{\infty} G_{ij}(\mathbf{x} - nL\mathbf{e}_1, \mathbf{y}) e^{in\beta}, \quad (70)$$

where G_{ij} is the fundamental solution for the two-dimensional elastodynamics, expressed by

$$\begin{aligned} G_{ij}(\mathbf{x}, \mathbf{y}) &= \frac{i}{4\mu} \left[H_0^{(1)}(k_T |\mathbf{x} - \mathbf{y}|) \delta_{ij} \right. \\ &\quad \left. + \frac{1}{k_T^2} \frac{1}{\partial y_i \partial y_j} \left(H_0^{(1)}(k_T |\mathbf{x} - \mathbf{y}|) - H_0^{(1)}(k_L |\mathbf{x} - \mathbf{y}|) \right) \right], \end{aligned} \quad (71)$$

with the Hankel functions $H_n^{(1)}$ of the first kind and order n and wavenumbers

$$k_L = \omega \sqrt{\frac{\rho}{\lambda + 2\mu}}, \quad (72)$$

$$k_T = \omega \sqrt{\frac{\rho}{\mu}}. \quad (73)$$

The lattice sum (70) would be the simplest expression of G_{ij}^p but has computational limitations. From (71), we see that G_{ij} asymptotically behaves as $G(\mathbf{x}, \mathbf{y}) = O(|\mathbf{x} - \mathbf{y}|^{-1/2})$ when $|\mathbf{x} - \mathbf{y}|$ tends to the infinity if $\text{Im}[\lambda] = \text{Im}[\mu] = 0$. This implies that the convergence speed of the lattice sum (70) is extremely slow; thus we require another representation of G_{ij}^p whose convergence is guaranteed and rapid.

For now, we assume that $x_2 - y_2 \neq 0$ and consider the following Fourier transform of the fundamental solution $G_{ij}(\mathbf{x}, \mathbf{y})$ with respect to x_1 :

$$\begin{aligned} \mathcal{F}_1[G_{ij}](\xi, x_2, \mathbf{y}) &:= \int_{-\infty}^{\infty} G_{ij}(\mathbf{x}, \mathbf{y}) e^{-i\xi x_1} dx_1 \\ &= \begin{cases} \frac{i}{2(\lambda+2\mu)\sqrt{k_L^2 - \xi^2}} d_i^{L+}(\xi) d_j^{L+}(\xi) \\ \times e^{ik_L(-p_1^{L+}(\xi)y_1 + p_2^{L+}(\xi)(x_2 - y_2))} \\ + \frac{i}{2\mu\sqrt{k_T^2 - \xi^2}} d_i^{T+}(\xi) d_j^{T+}(\xi) \\ \times e^{ik_T(-p_1^{T+}(\xi)y_1 + p_2^{T+}(\xi)(x_2 - y_2))} & (x_2 - y_2 > 0) \\ \frac{i}{2(\lambda+2\mu)\sqrt{k_L^2 - \xi^2}} d_i^{L-}(\xi) d_j^{L-}(\xi) \\ \times e^{ik_L(-p_1^{L-}(\xi)y_1 + p_2^{L-}(\xi)(x_2 - y_2))} \\ + \frac{i}{2\mu\sqrt{k_T^2 - \xi^2}} d_i^{T-}(\xi) d_j^{T-}(\xi) \\ \times e^{ik_T(-p_1^{T-}(\xi)y_1 + p_2^{T-}(\xi)(x_2 - y_2))} & (x_2 - y_2 < 0) \end{cases}, \end{aligned} \quad (74)$$

where $\mathbf{p}^{\text{L}\pm}(\xi)$, $\mathbf{d}^{\text{L}\pm}(\xi)$, $\mathbf{p}^{\text{T}\pm}(\xi)$, and $\mathbf{d}^{\text{T}\pm}(\xi)$ are defined as follows:

$$\mathbf{p}^{\text{L}\pm}(\xi) = \mathbf{d}^{\text{L}\pm}(\xi) = \frac{1}{k_{\text{L}}} \begin{pmatrix} \xi \\ \pm\sqrt{k_{\text{L}}^2 - \xi^2} \end{pmatrix}, \quad (75)$$

$$\mathbf{p}^{\text{T}\pm}(\xi) = \frac{1}{k_{\text{T}}} \begin{pmatrix} \xi \\ \pm\sqrt{k_{\text{T}}^2 - \xi^2} \end{pmatrix}, \quad (76)$$

$$\mathbf{d}^{\text{T}\pm}(\xi) = \frac{1}{k_{\text{T}}} \begin{pmatrix} \pm\sqrt{k_{\text{T}}^2 - \xi^2} \\ -\xi \end{pmatrix}. \quad (77)$$

Using Poisson's summation formula, the lattice sum (70) can be converted into the following series:

$$G_{ij}^{\text{p}}(\mathbf{x}, \mathbf{y}) = \begin{cases} G_{ij}^{p+}(\mathbf{x}, \mathbf{y}) & (x_2 - y_2 > 0) \\ G_{ij}^{p-}(\mathbf{x}, \mathbf{y}) & (x_2 - y_2 < 0) \end{cases}, \quad (78)$$

$$\begin{aligned} G_{ij}^{p\pm}(\mathbf{x}, \mathbf{y}) &= \sum_{n=-\infty}^{\infty} G_{ij}(\mathbf{x} - nL\mathbf{e}_1, \mathbf{y}) e^{in\beta} \\ &= \frac{1}{L} \sum_{m=-\infty}^{\infty} e^{i\xi_m x_1} \mathcal{F}_1[G_{ij}](\xi_m, x_2, \mathbf{y}) \\ &= \frac{i}{2L} \sum_{m=-\infty}^{\infty} \left(F_{ij}^{\text{L}\pm}(\xi_m) e^{ik_{\text{L}}(\mathbf{x}-\mathbf{y}) \cdot \mathbf{p}_m^{\text{L}\pm}} \right. \\ &\quad \left. + F_{ij}^{\text{T}\pm}(\xi_m) e^{ik_{\text{T}}(\mathbf{x}-\mathbf{y}) \cdot \mathbf{p}_m^{\text{T}\pm}} \right), \end{aligned} \quad (79)$$

where $\mathbf{p}_m^{\text{L}\pm} = \mathbf{p}^{\text{L}\pm}(\xi_m)$, $\mathbf{d}_m^{\text{L}\pm} = \mathbf{d}^{\text{L}\pm}(\xi_m)$, $\mathbf{p}_m^{\text{T}\pm} = \mathbf{p}^{\text{T}\pm}(\xi_m)$, $\mathbf{d}_m^{\text{T}\pm} = \mathbf{d}^{\text{T}\pm}(\xi_m)$, and

$$\xi_m = (\beta + 2m\pi)/L, \quad (80)$$

$$F_{ij}^{\text{L}\pm}(\xi_m) = \frac{1}{(\lambda + 2\mu)\sqrt{k_{\text{L}}^2 - \xi_m^2}} d_i^{\text{L}\pm}(\xi_m) d_j^{\text{L}\pm}(\xi_m), \quad (81)$$

$$F_{ij}^{\text{T}\pm}(\xi_m) = \frac{1}{\mu\sqrt{k_{\text{T}}^2 - \xi_m^2}} d_i^{\text{T}\pm}(\xi_m) d_j^{\text{T}\pm}(\xi_m). \quad (82)$$

The series (79) converges rapidly because of the exponential functions unless $|x_2 - y_2|$ becomes zero; otherwise the summands become $O(|m|^{-1})$ as $|m| \rightarrow \infty$. We can improve this convergence rate by using Kummer's transformation and

obtain

$$G_{ij}^P(\mathbf{x}, \mathbf{y}) = \sum_{s=1}^{N_K} c_s \sum_{n=-\infty}^{\infty} \tilde{G}_{ij}(\mathbf{x} - nL\mathbf{e}_1, \mathbf{y}; \sqrt{q_s}) e^{in\beta} + \sum_{m=-\infty}^{\infty} \hat{G}_{ij}(\mathbf{x}, \mathbf{y}, \xi_m), \quad (83)$$

$$\hat{G}_{ij}(\mathbf{x}, \mathbf{y}, \xi_m) = \begin{cases} \hat{G}_{ij}^+(\mathbf{x}, \mathbf{y}, \xi_m) & (x_2 - y_2 \leq 0) \\ \hat{G}_{ij}^-(\mathbf{x}, \mathbf{y}, \xi_m) & (x_2 - y_2 \geq 0) \end{cases}, \quad (84)$$

$$\begin{aligned} \hat{G}_{ij}^{\pm}(\mathbf{x}, \mathbf{y}, \xi_m) &= \frac{i}{2L} \left[F_{ij}^{\text{L}\pm}(\xi_m) e^{ik_{\text{L}} \mathbf{p}_m^{\text{L}\pm} \cdot (\mathbf{x} - \mathbf{y})} \right. \\ &\quad \left. + F_{ij}^{\text{T}\pm}(\xi_m) e^{ik_{\text{T}} \mathbf{p}_m^{\text{T}\pm} \cdot (\mathbf{x} - \mathbf{y})} \right] \\ &+ \sum_{s=1}^{N_K} \left(\tilde{F}_{ij}^{\text{L}\pm}(\xi_m) e^{-\sqrt{q_s} k_{\text{L}} \tilde{\mathbf{p}}_m^{\text{L}\pm} (\sqrt{q_s}) \cdot (\mathbf{x} - \mathbf{y})} \right. \\ &\quad \left. + \tilde{F}_{ij}^{\text{T}\pm}(\xi_m) e^{-\sqrt{q_s} k_{\text{T}} \tilde{\mathbf{p}}_m^{\text{T}\pm} (\sqrt{q_s}) \cdot (\mathbf{x} - \mathbf{y})} \right], \end{aligned} \quad (85)$$

where the vectors and functions with the tilde symbol are defined by replacing (λ, μ) with $(-\lambda/q_s, -\mu/q_s)$ (correspondingly $(k_{\text{L}}, k_{\text{T}})$ with $(i\sqrt{q_s}k_{\text{L}}, i\sqrt{q_s}k_{\text{T}})$). We can easily show that the summands of the first series in (83) become at worst (i.e. when $|x_2 - y_2| = 0$) $O(|m|^{-2N_K-1})$ as $|m| \rightarrow \infty$ when $q_s > 0$ and c_s solve the following linear system:

$$\begin{bmatrix} q_1 & q_2 & \cdots & q_{N_K} \\ q_1^2 & q_2^2 & \cdots & q_{N_K}^2 \\ \vdots & \vdots & \text{dots} & \vdots \\ q_1^{N_K} & q_2^{N_K} & \cdots & q_{N_K}^{N_K} \end{bmatrix} \begin{pmatrix} c_1 \\ c_2 \\ \vdots \\ c_{N_K} \end{pmatrix} = \begin{pmatrix} 1 \\ -1 \\ \vdots \\ (-1)^{N_K+1} \end{pmatrix}. \quad (86)$$

Thus, we determine c_s by solving (86); $q_s > 0$ are regarded as parameters. Note that (85) would suffer from a cancellation of significant digits in this case and thus require some transformations such as $e^z - 1 = -2ie^{z/2} \sin(iz/2)$. On the other hand, the first series in (83) always converges rapidly since $\tilde{G}_{ij}(\mathbf{x}, \mathbf{y}) = O(e^{-k|\mathbf{x}-\mathbf{y}|})$ ($k > 0$) as $|\mathbf{x} - \mathbf{y}| \rightarrow \infty$. Note that the representation (83)–(85) holds even if $x_2 - y_2 = 0$ though we assumed otherwise. For more details, refer to [19].

A.2 Far-field characteristics

The periodic Green's function expressed by (79) implies that a scattered field can be expanded into a sum of plane P- and S-waves. This can be shown by substituting (79) into the representation formula [31]

$$u_i(\mathbf{x}) = u_i^{\text{in}}(\mathbf{x}) + \int_{\Gamma} \left(C_{kljm} G_{ki,l}^P(\mathbf{x}, \mathbf{y}) n_m(\mathbf{y}) u_j(\mathbf{y}) \right. \\ \left. - G_{ij}^P(\mathbf{x}, \mathbf{y}) t_j(\mathbf{y}) \right) d\Gamma_y \quad \mathbf{x} \in U \setminus \bar{\Omega}, \quad (87)$$

which yields the plane-wave expansion (17) and formulae (21) and (22).

B Boundary element method

We describe the numerical solution of the periodic scattering problem (9)–(15). We first convert it into the Burton-Miller-type boundary integral equations [32]:

$$\left\{ \left[\left(\frac{1}{2} \mathcal{I} + \mathcal{D} \right) + \alpha \mathcal{N} \right] \mathbf{u} \right\}_i - \left\{ \left[\mathcal{S} - \alpha \left(\frac{1}{2} \mathcal{I} - \mathcal{D}^* \right) \right] \mathbf{t} \right\}_i = u_i^{\text{in}} + \alpha C_{ijkl} u_{k,l}^{\text{in}} n_j, \quad (88)$$

$$\left[\left(\frac{1}{2} \mathcal{I} - \mathcal{D}' \right) \mathbf{u} \right]_i + (\mathcal{S}' \mathbf{t})_i = 0, \quad (89)$$

where \mathcal{I} is the identity operator, and \mathcal{S} , \mathcal{D} , \mathcal{D}^* , and \mathcal{N} are the integral operators defined by

$$(\mathcal{S}\phi)_i(\mathbf{x}) = \int_{\Gamma} G_{ij}^p(\mathbf{x}, \mathbf{y}) \phi_j(\mathbf{y}) d\Gamma_y, \quad (90)$$

$$(\mathcal{D}\phi)_i(\mathbf{x}) = -\text{v.p.} \int_{\Gamma} C_{kljm} G_{ki,l}^p(\mathbf{x}, \mathbf{y}) n_m(\mathbf{y}) \phi_j(\mathbf{y}) d\Gamma_y, \quad (91)$$

$$(\mathcal{D}^*\phi_i)(\mathbf{x}) = \text{v.p.} \int_{\Gamma} C_{kljm} G_{ki,l}^p(\mathbf{x}, \mathbf{y}) n_m(\mathbf{x}) \phi_j(\mathbf{y}) d\Gamma_y, \quad (92)$$

$$(\mathcal{N}\phi_i)(\mathbf{x}) = -\text{p.f.} \int_{\Gamma} C_{impq} C_{kljn} G_{kp,lq}^p(\mathbf{x}, \mathbf{y}) n_m(\mathbf{x}) \times n_n(\mathbf{y}) \phi_j(\mathbf{y}) d\Gamma_y, \quad (93)$$

and \mathcal{S}' and \mathcal{D}' are defined by replacing (ρ, λ, μ) in \mathcal{S} and \mathcal{D} with (ρ', λ', μ') , respectively. Further, ‘v.p.’ and ‘p.f.’ stand for Cauchy’s principal value and the finite part of divergent integrals, respectively. The coupling parameter $\alpha \in \mathbb{C}$ is arbitrary if it has a non-zero imaginary part, but the best condition number of the boundary integral equations (88) and (89) is often achieved when $\alpha = -i/(\mu k_T)$ [33].

The boundary integral equations (88) and (89) are numerically solved after being discretised by a collocation method with piecewise constant elements, which results in a system of linear equations with a fully populated coefficient matrix. To reduce the computational cost of the linear algebraic operations, we apply the \mathcal{H} -matrix method [34] to the coefficient matrix and solve the linear system by an accelerated LU factorisation.

Acknowledgements

This work was supported by JSPS KAKENHI Grant Numbers JP19J21766, JP19H00740, JP17K14146. This is a post-peer-review, pre-copyedit version of an article published in Structural and Multidisciplinary Optimization. The final authenticated version is available online at: <http://dx.doi.org/10.1007/s00158-020-02689-y>.

References

- [1] Caloz, C. and Itoh, T. *Electromagnetic metamaterials: transmission line theory and microwave applications*. John Wiley & Sons, 2005.

- [2] Zhang, L., Mei, S., Huang, K., and Qiu, C.W. Advances in Full Control of Electromagnetic Waves with Metasurfaces. *Advanced Optical Materials*, Vol. 4, No. 6, pp. 818–833, 2016.
- [3] Yablonovitch, E. Photonic band-gap structures. *J. Opt. Soc. Am. B*, Vol. 10, No. 2, pp. 283–295, 1993.
- [4] Zhou, X., Liu, X., and Hu, G. Elastic metamaterials with local resonances: an overview. *Theoretical and Applied Mechanics Letters*, Vol. 2, No. 4, p. 41001, 2012.
- [5] Zhou, X. and Hu, G. Acoustic wave transparency for a multilayered sphere with acoustic metamaterials. *Phys. Rev. E*, Vol. 75, No. 4, p. 46606, 2007.
- [6] Zhou, X., Hu, G., and Lu, T. Elastic wave transparency of a solid sphere coated with metamaterials. *Physical Review B*, Vol. 77, No. 2, p. 24101, 2008.
- [7] Ambati, M., Fang, N., Sun, C., and Zhang, X. Surface resonant states and superlensing in acoustic metamaterials. *Phys. Rev. B*, Vol. 75, No. 19, p. 195447, 2007.
- [8] Liu, Z., Zhang, X., Mao, Y., Zhu, Y.Y., Yang, Z., Chan, C.T., and Sheng, P. Locally Resonant Sonic Materials. *Science*, Vol. 289, No. 5485, pp. 1734–1736, 2000.
- [9] Kweun, J.M., Lee, H.J., Oh, J.H., Seung, H.M., and Kim, Y.Y. Transmodal Fabry-Pérot Resonance: Theory and Realization with Elastic Metamaterials. *Phys. Rev. Lett.*, Vol. 118, No. 20, p. 205901, 2017.
- [10] Sigmund, O. and Jensen, J.S. Systematic design of phononic band-gap materials and structures by topology optimization. *Philosophical Transactions of the Royal Society of London. Series A: Mathematical, Physical and Engineering Sciences*, Vol. 361, No. 1806, pp. 1001–1019, 2003.
- [11] Bendsøe, M.P. and Kikuchi, N. Generating optimal topologies in structural design using a homogenization method. *Computer Methods in Applied Mechanics and Engineering*, Vol. 71, No. 2, pp. 197–224, 1988.
- [12] Diaz, A.R., Haddow, A.G., and Ma, L. Design of band-gap grid structures. *Structural and Multidisciplinary Optimization*, Vol. 29, No. 6, pp. 418–431, 2005.
- [13] Gazonas, G.A., Weile, D.S., Wildman, R., and Mohan, A. Genetic algorithm optimization of phononic bandgap structures. *International Journal of Solids and Structures*, Vol. 43, No. 18, pp. 5851–5866, 2006.
- [14] Dong, H.W., Su, X.X., Wang, Y.S., and Zhang, C. Topological optimization of two-dimensional phononic crystals based on the finite element method and genetic algorithm. *Structural and Multidisciplinary Optimization*, Vol. 50, No. 4, pp. 593–604, 2014.
- [15] Jensen, J.S. Topology optimization problems for reflection and dissipation of elastic waves. *Journal of sound and vibration*, Vol. 301, No. 1, pp. 319–340, 2007.

- [16] Christiansen, R.E. and Sigmund, O. Designing meta material slabs exhibiting negative refraction using topology optimization. *Structural and Multidisciplinary Optimization*, Vol. 54, No. 3, pp. 469–482, 2016.
- [17] Noguchi, Y., Yamada, T., Otomori, M., Izui, K., and Nishiwaki, S. An acoustic metasurface design for wave motion conversion of longitudinal waves to transverse waves using topology optimization. *Applied Physics Letters*, Vol. 107, No. 22, p. 221909, 2015.
- [18] Yang, X. and Kim, Y.Y. Topology optimization for the design of perfect mode-converting anisotropic elastic metamaterials. *Composite Structures*, Vol. 201, pp. 161–177, 2018.
- [19] Matsushima, K., Isakari, H., Takahashi, T., and Matsumoto, T. A boundary element method for two-dimensional elastic periodic scattering and its application to topology optimisation (in Japanese). *Transactions of the Japan Society for Computational Methods in Engineering*, No. 18, pp. 35–40, 2018.
- [20] Dong, H.W., Zhao, S.D., Wang, Y.S., and Zhang, C. Topology optimization of anisotropic broadband double-negative elastic metamaterials. *Journal of the Mechanics and Physics of Solids*, Vol. 105, pp. 54–80, 2017.
- [21] Dong, H.W., Zhao, S.D., Wang, Y.S., and Zhang, C. Broadband single-phase hyperbolic elastic metamaterials for super-resolution imaging. *Scientific Reports*, Vol. 8, No. 1, p. 2247, 2018.
- [22] Dong, H.W., Zhao, S.D., Wei, P., Cheng, L., Wang, Y.S., and Zhang, C. Systematic design and realization of double-negative acoustic metamaterials by topology optimization. *Acta Materialia*, Vol. 172, pp. 102–120, 2019.
- [23] Cadman, J.E., Zhou, S., Chen, Y., and Li, Q. On design of multi-functional microstructural materials. *Journal of Materials Science*, Vol. 48, No. 1, pp. 51–66, 2013.
- [24] Yi, G. and Youn, B.D. A comprehensive survey on topology optimization of phononic crystals. *Structural and Multidisciplinary Optimization*, Vol. 54, No. 5, pp. 1315–1344, 2016.
- [25] Amstutz, S. and Andrä, H. A new algorithm for topology optimization using a level-set method. *Journal of Computational Physics*, Vol. 216, No. 2, pp. 573–588, 2006.
- [26] Isakari, H., Takahashi, T., and Toshiro, M. A topology optimisation with level-sets of B-spline surface (in Japanese). *Transactions of the Japan Society for Computational Methods in Engineering*, Vol. 17, pp. 125–130, 2017.
- [27] Sokolowski, J. and Zochowski, A. On the topological derivative in shape optimization. *SIAM Journal on Control and Optimization*, Vol. 37, No. 4, pp. 1251–1272, 1999.
- [28] Bonnet, M. and Delgado, G. The topological derivative in anisotropic elasticity. *The Quarterly Journal of Mechanics and Applied Mathematics*, Vol. 66, No. 4, p. 557, 2013.

- [29] Amstutz, S. Analysis of a level set method for topology optimization. *Optimization Methods and Software*, Vol. 26, No. 4-5, pp. 555–573, 2011.
- [30] Eshelby, J.D. The determination of the elastic field of an ellipsoidal inclusion, and related problems. *Proceedings of the Royal Society of London A: Mathematical, Physical and Engineering Sciences*, Vol. 241, No. 1226, pp. 376–396, 1957.
- [31] Kitahara, M., Nakagawa, K., and Achenbach, J.D. Boundary-integral equation method for elastodynamic scattering by a compact inhomogeneity. *Computational Mechanics*, Vol. 5, No. 2, pp. 129–144, 1989.
- [32] Burton, A.J. and Miller, G.F. The application of integral equation methods to the numerical solution of some exterior boundary-value problems. In *Proceedings of the Royal Society of London A: Mathematical, Physical and Engineering Sciences*, Vol. 323, pp. 201–210. The Royal Society, 1971.
- [33] Matsushima, K., Isakari, H., Takahashi, T., and Matsumoto, T. An investigation of eigenfrequencies of boundary integral equations and the Burton-Miller formulation in two-dimensional elastodynamics. *International Journal of Computational Methods and Experimental Measurements*, Vol. 6, No. 6, pp. 1037–1127, 2018.
- [34] Bebendorf, M. *Hierarchical matrices*. Springer Berlin: Heidelberg, 2008.